Contrib Mineral Petrol (2017) 172:56
DOI 10.1007/s00410-017-1374-9

ORIGINAL PAPER

Mechanisms of fine extinction band development in vein quartz: new insights from correlative light and electron microscopy

Tine Derez[1] · Tom Van Der Donck[2] · Oliver Plümper[3] · Philippe Muchez[1] · Gill Pennock[3] · Martyn R. Drury[3] · Manuel Sintubin[1]

Received: 18 September 2016 / Accepted: 22 May 2017 / Published online: 5 June 2017

Abstract Fine extinction bands (FEBs) (also known as deformation lamellae) visible with polarized light microscopy in quartz consist of a range of nanostructures, inferring different formation processes. Previous transmission electron microscopy studies have shown that most FEB nanostructures in naturally deformed quartz are elongated subgrains formed by recovery of dislocation slip bands. Here we show that three types of FEB nanostructure occur in naturally deformed vein quartz from the low-grade metamorphic High-Ardenne slate belt (Belgium). Prismatic oriented FEBs are defined by bands of dislocation walls. Dauphiné twin boundaries present along the FEB boundaries probably formed after FEB formation. In an example of two sub-rhombohedral oriented FEBs, developed as two sets in one grain, the finer FEB set consists of elongated subgrains, similar to FEBs described in previous transmission electron microscopy studies. The second wider FEB set consists of bands with different dislocation density and fluid-inclusion content. The wider FEB set is interpreted as bands with different plastic strain associated with the primary growth banding of the vein quartz grain. The nanometre-scale fluid inclusions are interpreted to have formed from structurally bounded hydroxyl groups that moreover facilitated formation of the elongate subgrains. Larger fluid inclusions aligned along FEBs are explained by fluid-inclusion redistribution along dislocation cores. The prismatic FEB nanostructure and the relation between FEBs and growth bands have not been recognized before, although related structures have been reported in experimentally deformed quartz.

Keywords Nanostructures · Fine extinction band (FEB) · Fluid inclusion · Low-temperature tectonic deformation · Quartz intracrystalline deformation microstructures

Introduction

Densely spaced, intragranular, sub-planar microstructures visible with polarized light microscopy are widespread in quartz deformed at (sub-)greenschist conditions (Christie and Raleigh 1959; Blenkinsop and Drury 1988; Derez

Communicated by Steven Reddy.

Electronic supplementary material The online version of this article (doi:10.1007/s00410-017-1374-9) contains supplementary material, which is available to authorized users.

✉ Manuel Sintubin
manuel.sintubin@kuleuven.be

Tine Derez
tine.derez@gmail.com

Tom Van Der Donck
Tom.VanDerDonck@kuleuven.be

Oliver Plümper
O.Plumper@uu.nl

Philippe Muchez
philippe.muchez@kuleuven.be

Gill Pennock
G.M.Pennock@uu.nl

Martyn R. Drury
M.R.Drury@uu.nl

[1] Department of Earth and Environmental Sciences, KU Leuven, Celestijnenlaan 200E, 3001 Leuven, Belgium

[2] Department of Materials Engineering, KU Leuven, Kasteelpark Arenberg 44, 3001 Leuven, Belgium

[3] Department of Earth Sciences, Utrecht University, PO Bus 80.021, 3508 TA Utrecht, The Netherlands

et al. 2015). These microstructures are commonly known as deformation lamellae. Derez et al. (2015) and Trepmann and Stöckhert (2013), however, introduced new terminology. In the non-genetic scheme for quartz intragranular microstructures of Derez et al. (2015), deformation lamellae are termed fine extinction bands (FEBs). Trepmann and Stöckhert (2013), on the other hand, use the term short wavelength undulatory extinction (SWUE) to describe subplanar structures that are formed by cyclic deformation in the seismically active upper crust. In this paper we will use the term fine extinction bands. FEBs have been related to a range of nanostructures and associated genetic interpretations (Table 1), indicating that the microstructures observed at the scale of polarized light microscopy can be explained by a wide variety of crystallographic defects (Derez et al. 2015). Using TEM, natural FEBs have dominantly been identified as elongate subgrains bounded by curved dislocation walls containing well-ordered arrays of two to three sets of dislocations (McLaren et al. 1970; McLaren and Hobbs 1972; White 1973; Blenkinsop and Drury 1988; Drury 1993; Trepmann and Stöckhert 2003; Vernooij and Langenhorst 2005). McLaren and Hobbs (1972) further noted the occurrence of voids along the FEB boundaries. White (1973) also found other structures associated with FEBs in vein quartz including deformation twins, fractures and dislocations in slip bands. Experimentally formed FEBs in synthetic quartz have also been identified as elongate subgrains (McLaren et al. 1970), though also as alternating zones with high and low concentration of tangled dislocations (McLaren et al. 1970; Twiss 1974; Morrison-Smith et al. 1976), as walls of poorly ordered dislocations (Trepmann and Stöckhert 2013), and as amorphous bands (Christie and Ardell 1974).

Recently, a variable FEB morphology in polarized light microscopy has been discussed by Derez et al. (2015). FEBs can have a variable width (mostly <5 μm thick using polarized light microscopy), continuity, shape, extinction angles (~5°) and inclusion densities (Derez et al. 2015). How the FEB morphology is related to the specific nanostructures is not resolved in sufficient detail at the moment. Further, the presence of fluid inclusions is generally accepted to facilitate FEB formation (Tarantola et al. 2010), but the origin of fluid inclusions in FEBs is still disputed. In this paper, the relation between the FEB morphology and the associated nanostructure is therefore assessed by studying FEBs with polarized light microscopy, universal stage and an integrated electron microscopy approach. This integrated methodology has been proven successful in studying the kinematics of planar deformation features by Hamers et al. (2016, 2017).

We were able to show that FEBs are related to elongate subgrains, on the one hand, and to two previously unidentified nanostructures, on the other. The formation processes of these different nanostructures are compared to FEB formation processes suggested in the literature. In addition, new insights are gained in the relationship between fluid-inclusion distribution and FEBs.

Geological setting

The vein quartz studied comes from the High-Ardenne slate belt (HASB) (Fig. 1a), which is part of the Rhenohercynian foreland fold-and-thrust belt located at the northern

Table 1 Summary of the deformation mechanisms suggested for FEB formation

Brittle mechanisms	
Fracturing and healing	Becke (1892), *Den Brok* (1992), White (1973)
Shear	Christie and Raleigh (1959), Ingerson and Tuttle (1945), Turner (1948)
Crystal-plastic mechanisms	
Large variety of slip planes	*Heard and Carter* (1968), *Ord and Hobbs* (2011)
Twinning	Judd (1888)
Translation gliding	Savul and Mircea (1948)
Basal <a> slip for sub-basal FEBs and prism <c> slip for sub-prism FEBs	*Carter and Friedman* (1965), *Christie et al.* (1964)
Basal <a> slip in combination with Brazil twins	*McLaren et al.* (1967), White (1973)
Basal <a> slip in combination with recovery	*Christie and Ardell* (1974), *Drury* (1993), *Vernooij* (2005), *Vernooij and Langenhorst* (2005)
Basal <a> slip in growth layers	*Blacic* (1975)
Other mechanisms	
Shear melting	*Christie and Ardell* (1974)

References to experimental studies are italicized

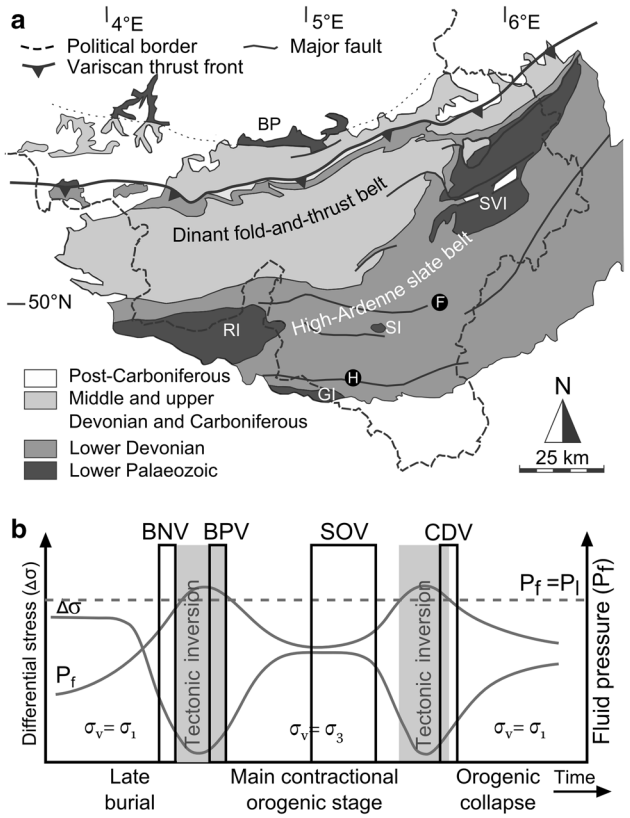

Fig. 1 **a** Geological map of Southern Belgium showing the main tectonostratigraphical units and the sample locations: (F) Fosset (50°01′25″N, 5°33′48″E, WGS84) (sample FOS1) and (H) Herbeumont (49°47′51″N, 5°13′17″E, WGS84) (sample HB08HV13). *BP* Brabant Parautochton, *GI*, *RI*, *SI*, *SVI* Givonne, Rocroi, Serpont and Stavelot-Venn basement inlier, respectively. **b** Timing of veining in the HASB with respect to the tectonic inversions related to the Variscan orogeny. The differential stress and fluid pressure evolution are tentatively indicated (after Depoorter et al. 2014). *BNV* bedding-normal veins (Van Noten et al. 2012), *BPV* bedding-parallel veins (Van Noten et al. 2012), *CDV* cleavage-discordant veins (Depoorter et al. 2014; Van Baelen 2010), *SOV* syn-orogenic veins (Jacques et al. 2014), $\Delta\sigma$ differential stress, σ_v vertical stress, σ_1, σ_3 maximum and minimum principal stress, respectively, P_f fluid pressure, P_l lithostatic pressure

extremity of the late Palaeozoic Central European Variscan orogenic belt (Oncken et al. 1999). The metasediments in the HASB were deformed from the late Visean until the early Moscovian (325–310 Ma) under sub-greenschist conditions (Fielitz and Mansy 1999). The HASB contains several quartz vein generations that can be related to the tectonic stress inversions at the onset and during the latest stages of the Variscan orogeny (Fig. 1b).

FEBs are widespread in the vein quartz of all vein generations in the study area. This paper focuses on FEBs in a representative deformed quartz grain selected from both an early- and a late- to post-orogenic vein. In both samples a wide variety of FEB orientations with respect to the crystal lattice commonly occur in an individual grain (Derez et al. 2015). For the selected early-orogenic vein sample, FEBs were studied in 140 and 55 grains in the *x*–*y* and the *x*–*z* sections, respectively (Derez et al. 2016). In the second vein sample, 19 grains with FEBs were studied in detail with polarized light microscopy.

The first quartz grain is from a typical early-orogenic intermullion vein within a micaceous quartzite bed belonging to the early Devonian (Pragian) Anlier Formation in Fosset (Belgium) (sample FOS1) (Kenis et al. 2005). The quartz vein is oriented at a high angle to the bedding [bedding-normal vein (BNV) in Fig. 1b] as a result of a regional hydraulic fracturing event during the latest stages of burial, at the onset of the Variscan orogeny (Kenis et al. 2005; Van Noten et al. 2012). Early-orogenic bedding-normal veins were inferred to have formed at near-lithostatic fluid pressures between ~150 and ~250 MPa, based on microthermometry of primary fluid inclusions and on an independent chlorite geothermometer indicating veining around 390 °C (Kenis 2004).

The second quartz grain is taken from a late- to post-orogenic cleavage-discordant vein (CDV) in the La Fortelle Quarry, Herbeumont (Belgium) (sample HB08HV13) (Fig. 1b) within a fine-laminated pelite also belonging to the Anlier Formation (Van Baelen 2010). The vein formed in an extensional regime, after the main stage of the Variscan orogeny. Vein deformation resulted from cleavage-parallel shearing with generally top-to-the-south kinematics. Taking into account a geothermal gradient between 30 and 50 °C/km (Beugnies 1986; Schroyen and Muchez 2000), microthermometry on re-equilibrated and primary fluid inclusions indicates vein formation and deformation at sub-lithostatic fluid pressures below ~220 MPa and temperatures between ~270 and ~390 °C (Van Baelen 2010).

Methods

Standard 30-µm-thick thin sections were studied using polarized light microscopy and electron microscopy. The thin sections were polished to microprobe standards and further polished with a 0.02-µm colloidal silica suspension for an hour. Polarized light microscopy images were taken with a Leica DMLP light microscope equipped with a DP 200 camera linked with the Deltapix Viewer LE software package at the Department of Earth and Environmental Sciences of the KU Leuven.

The complete orientation of FEB planes with respect to the crystal lattice was measured using a combination of universal stage microscopy and electron backscatter diffraction (EBSD) and plotted in the new stereographic projection template of Ferrière et al. (2009). Using an Ernst Leitz Wetzlar Universal Stage (Department of

Earth and Environmental Sciences, KU Leuven) the orientation of the FEB plane was measured with respect to the sample reference frame. On the same location in the grain, crystallographic orientation data were obtained by EBSD orientation imaging microscopy with a FEI Nova NanoSEM 450 equipped with a field emission gun and with an Edax Hikari xp EBSD camera, at the Department of Materials Engineering of the KU Leuven. EBSD operating conditions used were low-vacuum mode, 15 mm working distance, 70° sample tilt and 20 kV acceleration voltage. The measurements were preformed on a hexagonal grid, with a step size of 1 µm. For the automated indexing and processing of the data, the TSL software OIM analysis 7 was used. A reference file for trigonal quartz was used, enabling identification of Dauphiné twin boundaries (DTBs). To improve the signal-to-noise ratio, the maps were processed with the Neighbour Confidence Index Correlation algorithm; changing the orientation of points with a confidence index below 0.1 into an average orientation of its directly neighbouring points, and the Neighbour Orientation Correlation algorithm; changing the orientation of points that do not belong to a grain with a set grain tolerance angle of 5° and a confidence index below 0.1 into an average orientation of its directly neighbouring points.

The FEBs were further characterized by means of electron probe micro-analyser cathodoluminescence (EPMA-CL) spectrometry with a JEOL xCLent spectrometer on a JEOL JXA-8530F FEG-EPMA at the Department of Earth Sciences of the Utrecht University. For CL acquisition 10 kV acceleration voltage, 20 nA beam current and a dwell time of 20 ms were used. The samples were carbon coated to prevent charging. The CL analyses were performed before any other electron microscopy, in order to have a fresh luminescent signal, undisturbed from previous electron imaging. With the JEOL xCLent software package, different wavelength ranges of the CL spectrum (in the red, green and blue ranges) have been manually selected around observed peaks in the spectrum. The intensities of the wavelengths are displayed in a grayscale.

Finally, the FEB nanostructure was investigated by transmission electron microscopy (TEM). Bright field overview images were taken with a FEI TECNAI 12 TEM at 120 kV, and more detailed images were taken with a FEI TECNAI 20F TEM at 200 kV, at the EM Square Microscopy Centre of the Utrecht University. TEM foils (~200 nm thick) were prepared, orthogonal to the thin sections, by focused ion beam milling with a Nova Nanolab 600 FEB-SEM at the Utrecht University. An additional protective layer of Pt was deposited on top of the layer of interest for the preparation of the TEM foil.

Results

FEB orientations

The FEB orientation data (universal stage measurements) are shown with respect to the crystal lattice frame (deduced with EBSD) in the new stereographic projection template of Ferrière et al. (2009). Eighty-eight per cent of the FEBs in sample FOS1 are parallel to {51–60} planes (within a 5° range) (Fig. 2a) and have a single sub-prismatic orientation. In the HB08HV13 sample, the orientation of one FEB set is scattered between the *r*-, *z*-, *ξ*- and *π*-planes, while the other FEB set is sub-parallel to the *z*- and *ξ*-crystal planes (Fig. 2b). Only 13% of the FEBs in the HB08HV13 sample are oriented within a 5° range of a crystal plane.

Prismatic FEBs

Polarized light microscopy

The prismatic FEBs in the FOS1 sample are particularly straight, alternating broad (~10 µm) and very thin (~2 µm) FEBs (Fig. 3a). Alternating FEBs show a difference in extinction angle up to 3°. Fluid inclusions are only observed at the intersection of the FEBs with fluid-inclusion planes (FIPs; a planar arrangement of fluid inclusions). Fluid inclusions forming part of a FIP are locally aligned parallel to the FEBs (Fig. 3b) and are concentrated in one of the alternating FEB sets (Fig. 3b).

EBSD analysis

The microstructure of the narrow and broad FEBs observed with light microscopy (Fig. 4a) is also clear in EBSD mapped data (Fig. 4b, c). Narrow FEBs tend to show poorer EBSD pattern quality. FEBs are bounded by low-angle boundaries, with misorientation angles between 2° and 6° (Fig. 4c, d). In some places, DTBs are aligned parallel to the FEB boundaries (DTB, Fig. 4c). In many places, small, patchy regions are indexed as DTBs, although these small regions are hard to distinguish from misindexing. Misorientation axes for the FEBs are shown in Fig. 4e for the angles between 3° and 5°.

CL spectrometry

A typical CL spectrum from an area with prismatic FEBs (Fig. 5) shows a high intensity in the red wavelength range (608–677 nm) and minor intensity in the blue (365–488 nm) and green (534–544 nm) wavelength ranges. CL and orientation contrast maps show the FEB

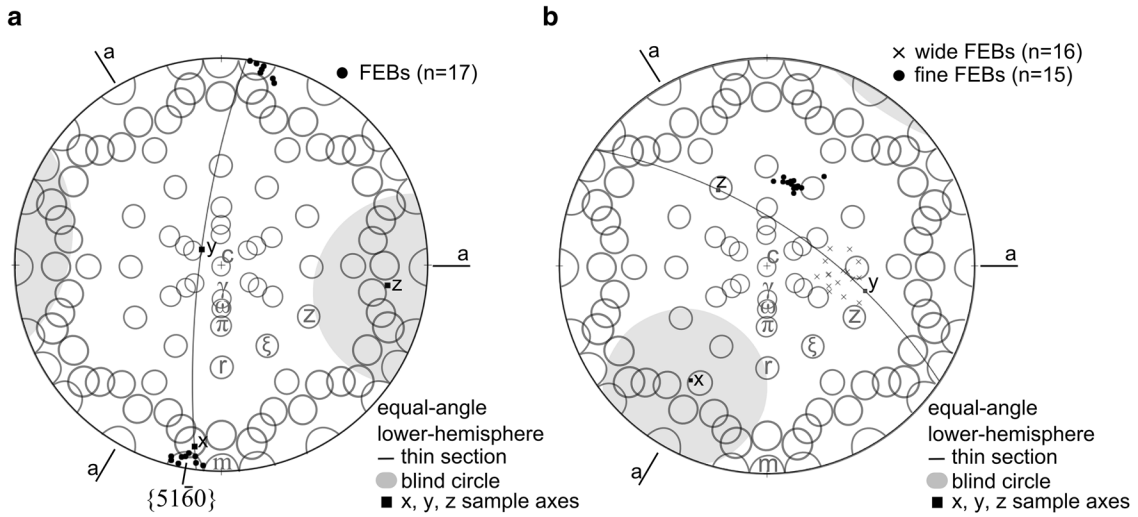

Fig. 2 FEB orientation with respect to the crystal lattice based on universal stage microscopy and EBSD. The poles to the FEB planes are plotted in a lower-hemisphere equal-angle projection. Crystal directions that have low Miller–Bravais indices are also indicated as circles with 5° radius. The location of the poles to the γ, ω, π, r, ξ, z and m planes is indicated. The *great circles* mark the orientation of the thin section of the studied grains. The *grey regions* mark the blind regions where FEB orientations cannot be measured because of a limited rotation in the universal stage. **a** FEBs in the selected grain in the *xy* section of sample FOS1 are close to the prismatic m planes. **b** FEBs in the selected grain in the *zy* section of sample HB08HV13 are close to rhombohedral planes. *n* number of FEBs plotted. Plot produced with OpenStereo 0.1.2

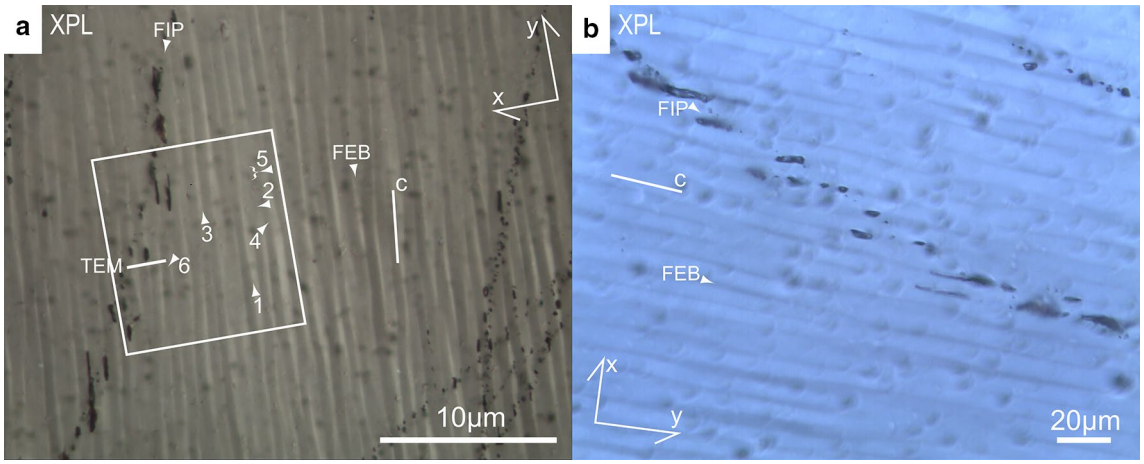

Fig. 3 Cross-polarized light (XPL) microscopy images of the prismatic FEBs in sample FOS1. The projection of the *c*-axis in the thin section plane is marked with a *thin line*, *c*. **a** *Lower magnification* image showing the location of the regions of Fig. 6 (*white rectangle*); the *arrows* correspond to those indicated in Fig. 6 and are referred to in the text. The location of the TEM foil is indicated with a *thick white solid line, TEM*. **b** Detailed image of the fluid-inclusion plane (FIP) showing the alignment of fluid inclusions along the FEBs

boundaries have stronger red and green intensity than the rest of the grain (Figs. 6a–c, arrow 1). The orientation contrast image shows alternate light and dark bands, consistent with the crystal lattice misorientations detected in the EBSD maps of a nearby area. Some bands terminate at orthogonal boundaries (Fig. 6a, arrow 2), while other bands have a lenticular geometry (Fig. 6a, arrow 3). The red and green CL further highlights small fluid-inclusion alignments (Fig. 6a, b, arrow 4). Weaker darker horizontal bands are also apparent in the red (and to a lesser extent, the green) CL image, one of which is shown by arrow 5 in Figs. 6b. Bands with a slightly brighter blue CL correspond to the brighter bands in the orientation contrast image (Fig. 6a, d, arrow 1).

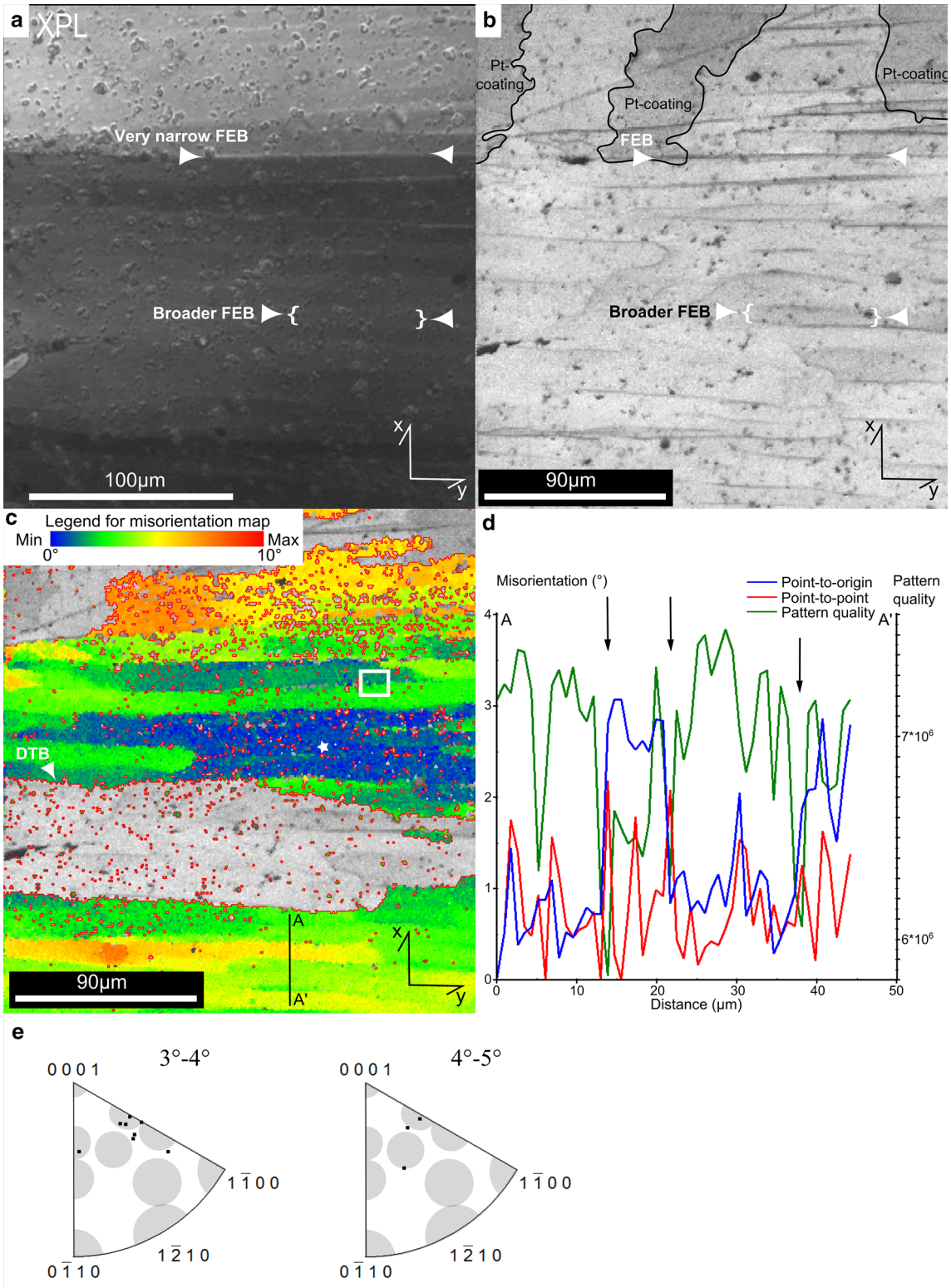

Fig. 4 EBSD data from prismatic FEBs in sample FOS1. **a** Polarized light microscopy image of the area in maps **b** and **c**. **b** Pattern quality map (areas of residual *Pt-coating* are indicated). **c** Misorientation map with maximum misorientation angle of 10° relative to a reference point indicated by a *white star*. Higher misoriented regions with a Dauphiné twin law (DTB) (180° rotation around the *c*-axis with tolerance angle of 5°) are indicated with *red lines*. The DTBs surrounding a few pixels can result from misindexing. **d** Misorientation profile *A*–*A′* indicated in the misorientation map (**c**). Interpreted FEB boundaries are indicated with *black arrows*. **e** Lower-hemisphere equal-angle inverse pole figures showing misorientation axes distribution for misorientation angles between 3° and 5°, calculated between all neighbouring points in the *white rectangle* in map (**c**)

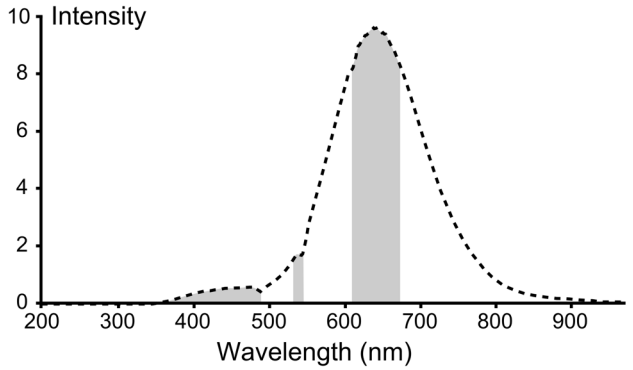

Fig. 5 CL spectrum of a point measured in the CL map of the prismatic FEBs in sample FOS1. *Grey regions* indicate the wavelength ranges used for the CL maps in Fig. 6 (614–671, 531–546, and 385–489 nm)

TEM analysis

The TEM section made across the prismatic FEBs shows four zones which have a higher dislocation density relative to the rest of the image (Fig. 7a). Zones 1–3 contain long narrow subgrains separated by sub-parallel subgrain boundaries. In addition to these elongate subgrain boundaries Fig. 7b also shows two parallel planar structures, each marked by displacement fringes parallel to the trace of the planar feature, typically found for DTBs (McLaren and Phakey 1969). A contrast change, associated with a misorientation difference across a subgrain boundary, is not observed in the regions either side of the twin planes, showing that both planar structures are pure twin boundaries. These twins correspond to the bright CL bands at an angle of ~45° to the left in Fig. 6b–d, arrow 6, that were not recognized as extinction bands with polarized light microscopy.

Although the TEM images show a superposition of all nanostructures present throughout the thickness of the TEM foil, the subgrain boundaries possibly end against a twin boundary (Fig. 7b, arrow 1), or link to other subgrain boundaries (Fig. 7c, arrow 1), or end in an area with a high dislocation density (Fig. 7c, arrow 2). The subgrain boundaries are often connected by individual dislocations (Fig. 7b, arrow 2 and Fig. 7c, arrow 3). Subgrain boundaries oriented at a low angle with respect to the TEM foil are visible as hexagonal patterns of dislocations (Fig. 7c, rectangle). In all zones, the dislocations are concentrated along the boundaries.

Contrary to zones 1–3, zone 4 consists of a single subgrain boundary containing well-aligned dislocations (Fig. 7d). Along this subgrain boundary many fluid inclusions occur, often having an elongate negative-crystal shape (Fig. 7e).

A comparison with the forescatter image (Fig. 6a) shows that zones 1 and 2 correspond to very narrow FEBs, while zones 3 and 4 represent FEB boundaries. The boundaries of these prismatic FEBs thus correspond to a single subgrain boundary or to a network of subgrains with a high dislocation density.

Sub-rhombohedral FEBs

Polarized light microscopy

The second quartz grain, sample HB08HV13, contains two FEB sets (Fig. 8). One FEB set is very straight, with a wide spacing and large 6° difference in extinction angle between the bands. The second more anastomozing FEB set has finer spacing and smaller extinction differences. Fluid inclusions are locally present along the FEBs, close to intersections between FEBs and FIPs.

EBSD analysis

In the EBSD maps, only the wider FEB set was detected in the form of low-angle subgrain boundaries along the FEB boundaries (Fig. 9).

CL spectrometry

In orientation contrast maps only the wider FEBs produced some contrast (Fig. 10a). In the corresponding CL maps both FEB sets are visible (Fig. 10b). In a CL map combining the red (577–710 nm) and the blue (378–483 nm) luminescence signal, FEBs occur as alternating red and blue bands (Fig. 10c). In case of the wider FEBs, this mainly results from a varying red(/green) intensity and a more continuous low blue intensity. The wider FEBs show an alternating bright–dull red(/green) luminescence (Fig. 10d, e). In case the red(/green) CL is more dull, sometimes the blue CL is more bright (Fig. 10d–f, arrows 1–3). These bands often have a lenticular shape and can have a slightly varying orientation. The fluid-inclusion-rich FEBs show a bright red CL signal (Figs. 8 arrow 4, 10d, arrow 4).

The finer FEBs are alternatingly dull and bright luminescent, in the red(/green) and blue wavelengths (Fig. 10d–f, arrows 5 and 6). The blue CL map additionally shows a darker region in the lower left corner (Fig. 10f, arrow 7).

TEM analysis

The TEM foil across the sub-rhombohedral FEBs has generally a much higher defect density than the prismatic FEBs. The foil is divided into five zones corresponding to the zones identified with CL. Zones 1, 3 and 5 correspond to the more red zones containing the finer FEBs, while zones 2 and 4 have a higher blue intensity (Figs. 10, 11a, b).

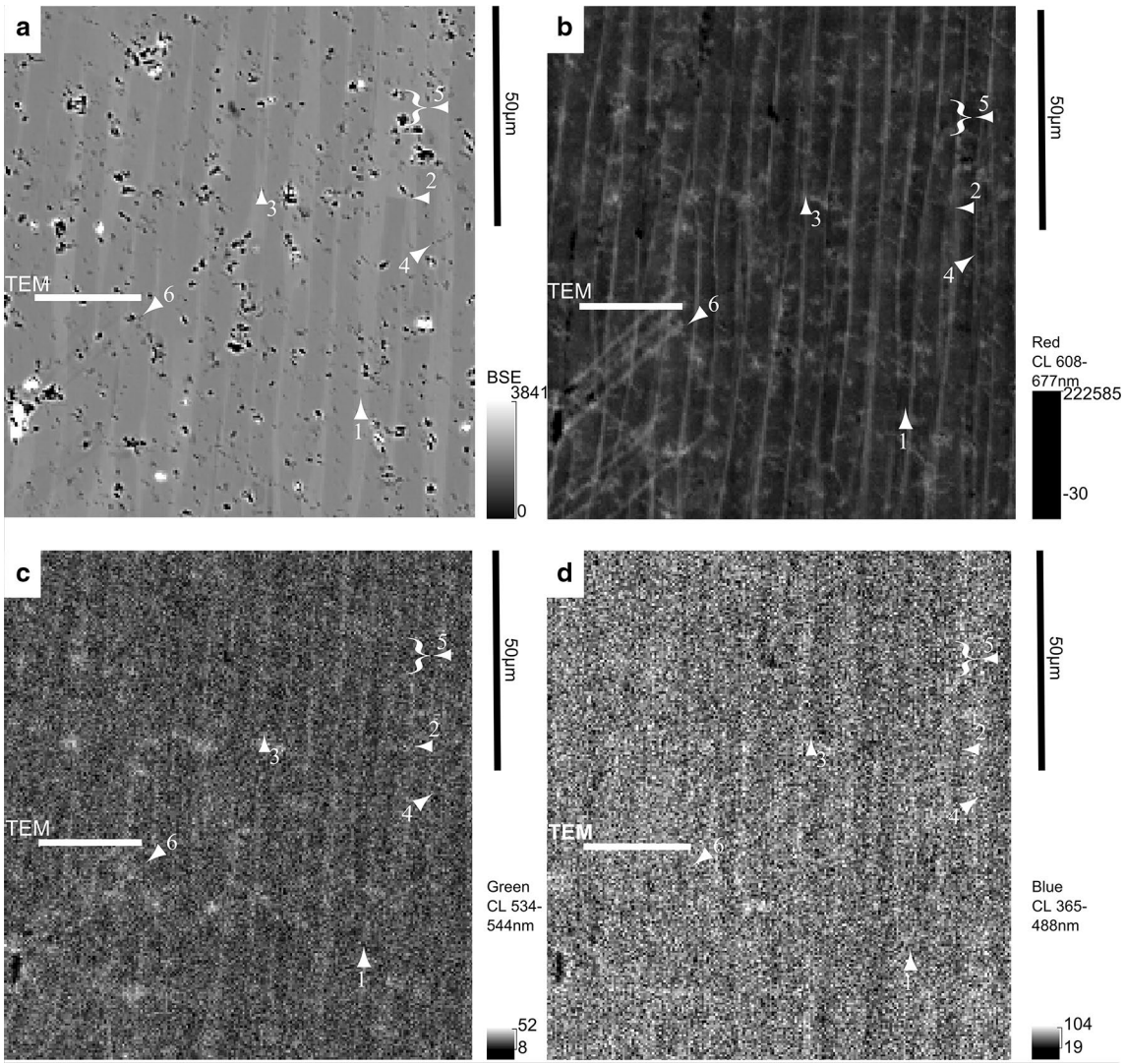

Fig. 6 CL analysis of prismatic FEBs in sample FOS1. **a** Forescatter image. **b–d** Maps displaying the measured intensity of selected ranges of wavelength bounding peaks in the spectrogram of the total mapped area (Fig. 5). The wavelength ranges are 614–671 nm (*red*), 531–546 nm (*green*) and 385–489 nm (*blue*), respectively. The intensities are displayed in a *grayscale*. The *arrows* serve as reference points for comparison with Fig. 3 and are referred to in the text. The location of the TEM section is indicated with a *thick white solid line, TEM*

Zones 1, 3 and 5 all contain lenticular subgrains with a variable elongation direction in the different zones (Fig. 12a, b). Dislocations occur in networks are often curved (Fig. 12b, c, arrows 1), and many dislocation loops are present (Fig. 12b, c, arrows 2). The dislocation arrangement in the boundaries varies from well-aligned (Fig. 12c, upper side of the subgrain boundary) to more tangled (Fig. 12c, bottom side of the subgrain boundary). In zone 5, some bands with fringes are interpreted as twins (Fig. 12d, brackets). These twins are sub-parallel to the subgrain boundaries and contain dislocations along them. In zones 1, 3 and 5 there is a high concentration of nanometre-scale fluid inclusions (Fig. 12b, c, arrows 3), and in zones 3 and 5 some fluid inclusions up to 200 nm wide are observed (Fig. 12a, d, arrows 1).

Zones 2 and 4 have a lower dislocation density than the other zones. Instead these zones contain parallel straight twin boundaries (Fig. 12e, f, arrows 1).

Interpretation

Prismatic FEBs

All techniques consistently show that the prismatic FEBs are bounded by a single subgrain boundary, or by a

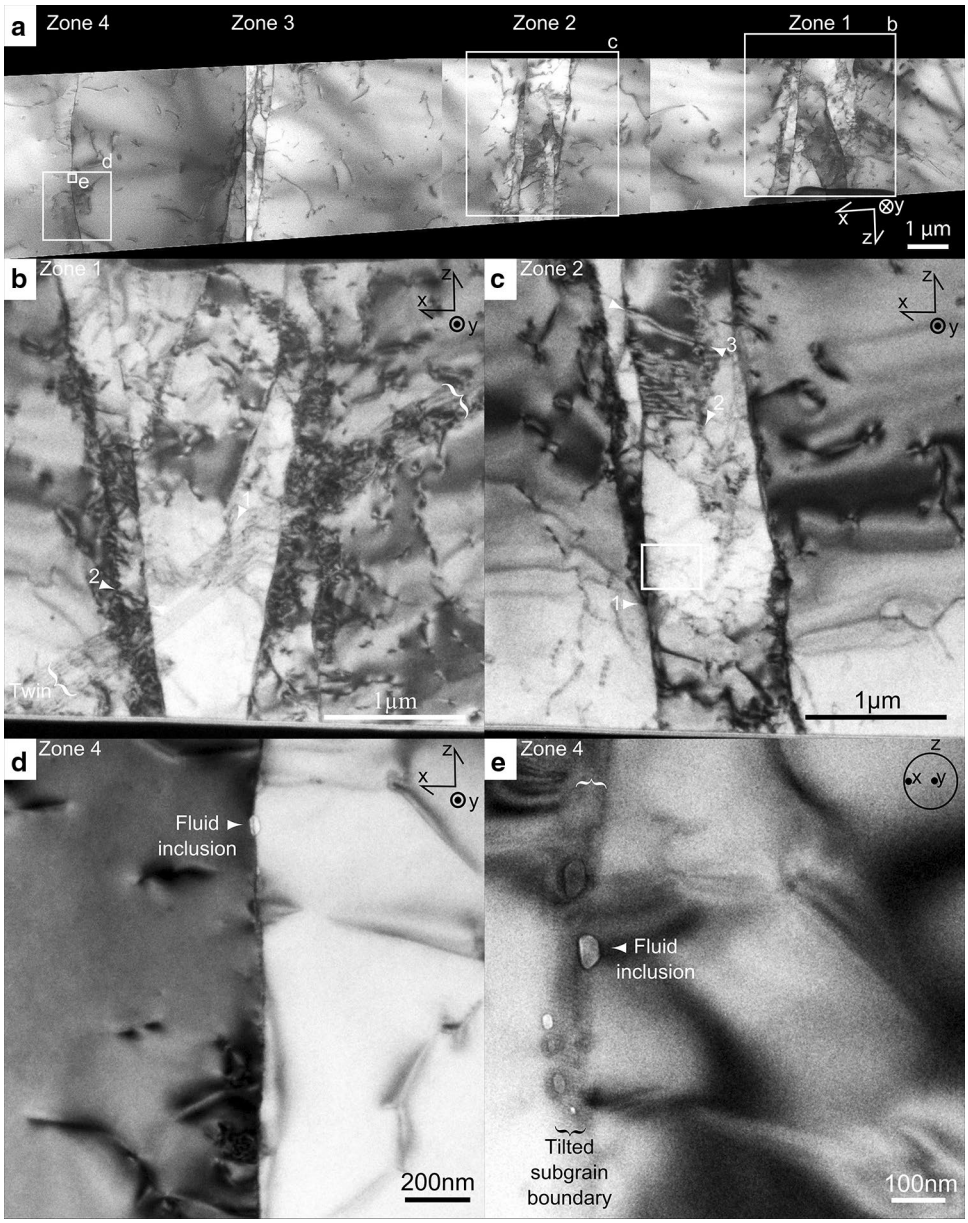

Fig. 7 TEM analyses of the prismatic FEBs in sample FOS1. **a** Overview bright field composite image of the complete TEM section. **b**–**e** Bright field images

band of subgrain boundaries, with misorientation angles mainly between 2° and 5°. These boundaries resulted in a red CL, in agreement with Hamers et al. (2017) and low EBSD pattern quality.

The prismatic FEB microstructure in this study forms as bands of sub-parallel subgrain boundaries. This microstructure differs to sub-basal FEBs described in the literature, in which single subgrain boundaries occur (e.g. Drury 1993; Trepmann and Stöckhert 2013). We suggest that the prismatic FEB structure is similar to transition bands in metals based on their similar morphology (e.g. Lobanov et al. 2013). The bands of closely spaced subgrain boundaries with high dislocation density correspond to the hinge zones of lattice folding, while the wider bands with low dislocation density correspond to the fold limbs. A wide hinge zone is formed in metals when the deformation occurs during cold-working. During subsequent annealing or stress relaxation the hinge zones recover into bands of subgrains. To form a transition band microstructure, some difference in slip activity is required to produce the lattice misorientations, which become concentrated in the hinge zones. Misorientation axes obtained from EBSD indicate that {r}<a> is the main slip system involved, assuming that the misorientation results from the presence of edge dislocations (Neumann 2000; Lloyd 2004). A micro-fold structure could develop, if slip on the {r}<a> system occurred on the same slip plane but with different shear sense on either side of the FEB boundary. Alternatively, activation of

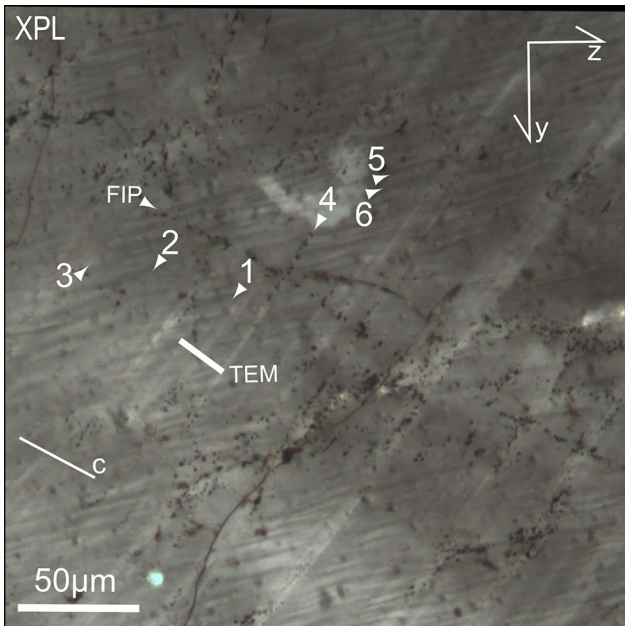

Fig. 8 Cross-polarized light (XPL) microscopy images of the sub-rhombohedral FEBs in sample HB08HV13. The projection of the *c*-axis in the thin section plane is marked with a *thin line*, *c*. The *arrows* correspond to those indicated in Fig. 10 and are referred to in the text. The location of the TEM foil is indicated with a *thick white solid line, TEM*. A fluid-inclusion plane (*FIP*) showing the alignment of fluid inclusions is indicated

different planes of the {r}<a> system would result in the build-up of lattice misorientations. If the FEB boundary consists of screw dislocations, the misorientation axes suggest a combination of {z}<a> and (c)<a> slip according to Lloyd (2004).

In metals a transition band structure is specifically developed by static recovery following cold-working deformation. In naturally deformed quartz, deformed in the upper crust, a history of high strain rate and high-stress deformation followed by stress relaxation, associated with the seismic cycle, will be common (Trepmann and Stöckhert 2013). Trepmann and Stöckhert (2013) showed that a specific type of FEB structure, i.e. SWUE, with prismatic, rhombohedral and basal orientations, is developed in "kick and cook" experiments, involving a low-strain, high-stress deformation, followed by deformation and recovery during stress relaxation. The prismatic FEB structure may be a natural analogue of SWUE produced by a "kick and cook" deformation history.

The prismatic FEBs are associated with DTBs, which are thought to have formed syn- to post-FEB formation since they are clearly influenced by the FEBs presence. The prismatic FEBs are generally not associated with fluid inclusions, as none are observed in the TEM zones 1–3 (Fig. 7). The fluid inclusions in the single subgrain boundary of zone 4 are therefore interpreted to be redistributed remnants of a FIP that is present near the TEM foil location. This is clearly indicated by the fluid-inclusion alignments along FEBs, observed with polarized light microscopy. Fluid-inclusion redistribution can take place by water leakage via pipe diffusion along dislocation cores as described by Bakker and Jansen (1994). In this way, the FEB boundaries with their high dislocation density can serve as pathways for fluid-inclusion redistribution.

Sub-rhombohedral FEBs

This example consists of two sub-rhombohedral FEB sets in a single grain, showing different spacing and misorientation, related to different nanostructures.

Within the wider FEBs (zones 1, 3 and 5 in Fig. 12), the finer FEBs consist of lenticular subgrains showing a weaker cathodoluminescence in both blue and red wavelengths. FEBs like this are common in quartz (McLaren and Hobbs 1972; White 1973; Blenkinsop and Drury 1988; Drury 1993; Trepmann and Stöckhert 2003, 2013), and in metals (Drury 1993 and references therein).

The formation of natural FEBs bounded by single subgrain boundaries have been explained in previous studies by recovery of slip bands with tangled dislocations, resulting from concentrated dislocation glide on a single slip system (Drury 1993; Trepmann and Stöckhert 2013). During dynamic recovery, the dislocations move out of the slip band by climb and cross-slip. The moving dislocations combine with other dislocations to constitute a new subgrain boundary parallel to the initial slip band (Drury 1993). This is a likely model for the elongate subgrains constituting the finer sub-rhombohedral FEBs. The dislocation network with the curved dislocations and the occurrence of dislocation loops are characteristic of a recovered structure in quartz (Drury 1993). The strong development of a recovered slip band structure suggests that the zones containing fine FEBs have accumulated high strains, on different slip planes.

The role of Dauphiné twinning in the formation of these lenticular subgrains is unclear and may be more important than previously acknowledged: DTBs can have been precursors for the observed subgrain boundaries [e.g. DTBs observed parallel to the subgrain boundaries in zone 5 (Fig. 12d)]. Further research is required to study this relation.

The lenticular subgrains identified with TEM could not be directly correlated with the polarized light microscopy or the EPMA-CL observations. At the micrometre-scale the FEBs are parallel and continuous, while the individual subgrains have irregular boundaries at the nanometre-scale. The FEBs, moreover, result from the superimposed effect of the nanostructure present throughout the whole thickness of the thin section, containing stacked subgrains. The effect

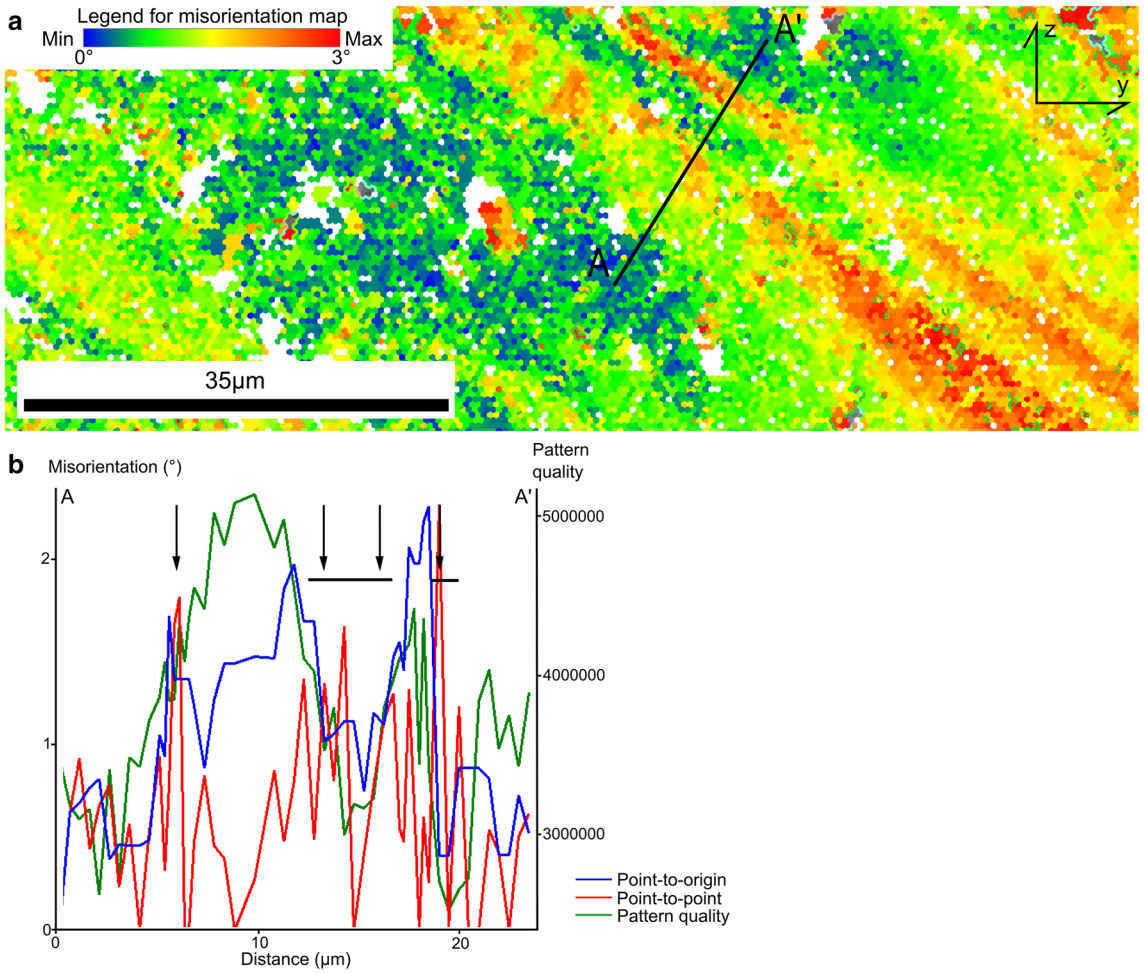

Fig. 9 EBSD data from sub-rhombohedral FEBs in sample HB08HV13. **a** Misorientation map with maximum misorientation angle of 3°; *white regions* show small misindexed regions. **b** Misorientation profile indicated in the misorientation map. Interpreted FEB boundaries are indicated with *black arrows*, though the uncertainty (*black horizontal lines*) on the boundary location is higher than for the prismatic FEBs (Fig. 4)

of the misorientation angle between subgrains is, therefore, unlikely to be resolved using polarized light microscopy.

The wider FEB set corresponds to elongated subgrains, with different defect microstructures in different bands. The blue luminescent zones 2 and 4 show a lower nanometre-scale fluid-inclusion content, dislocation density and development of the second set of fine FEBs than the red luminescent zones. Therefore, the strain level is inferred to be higher in the red luminescent zones. We suggest that this higher strain level can be induced by an initially higher structurally bounded hydroxyl concentration in the quartz, since numerous experimental studies on quartz single crystals have shown that strain concentrates in bands with a higher hydroxyl concentration (Blacic 1975; Morrison-Smith et al. 1976; McLaren et al. 1983; Mainprice and Jaoul 2009). In natural vein quartz, a variable grown-in hydroxyl content can be induced by variations in speed of crystal growth, resulting in growth banding typically parallel to the sub-rhombohedral crystal planes. The lattice misorientations between the growth bands can result from a varying slip activity between the growth bands (Blacic 1975; Morrison-Smith et al. 1976).

The nanometre-scale fluid inclusions in the inferred high hydroxyl or water content bands (zone 1, 3 and 5) are thought to have formed by clustering of structurally bounded hydroxyl groups. The model of fluid-inclusion formation from structurally bounded hydroxyl groups was originally based on the observations of fluid-inclusion formation during experimental heat treatment (above 600 °C at atmospheric pressure) of quartz (amethyst and citrine) (McLaren and Phakey 1966; McLaren and Retchford 1969; Morrison-Smith et al. 1976). Structurally bounded hydroxyl or hydrogen concentrations reported range from 10 to 10,000 H/10^6 Si in natural quartz, measured by infrared absorption spectrometry (Kilian et al. 2016). Based on the lowest and highest concentration of H atoms measured

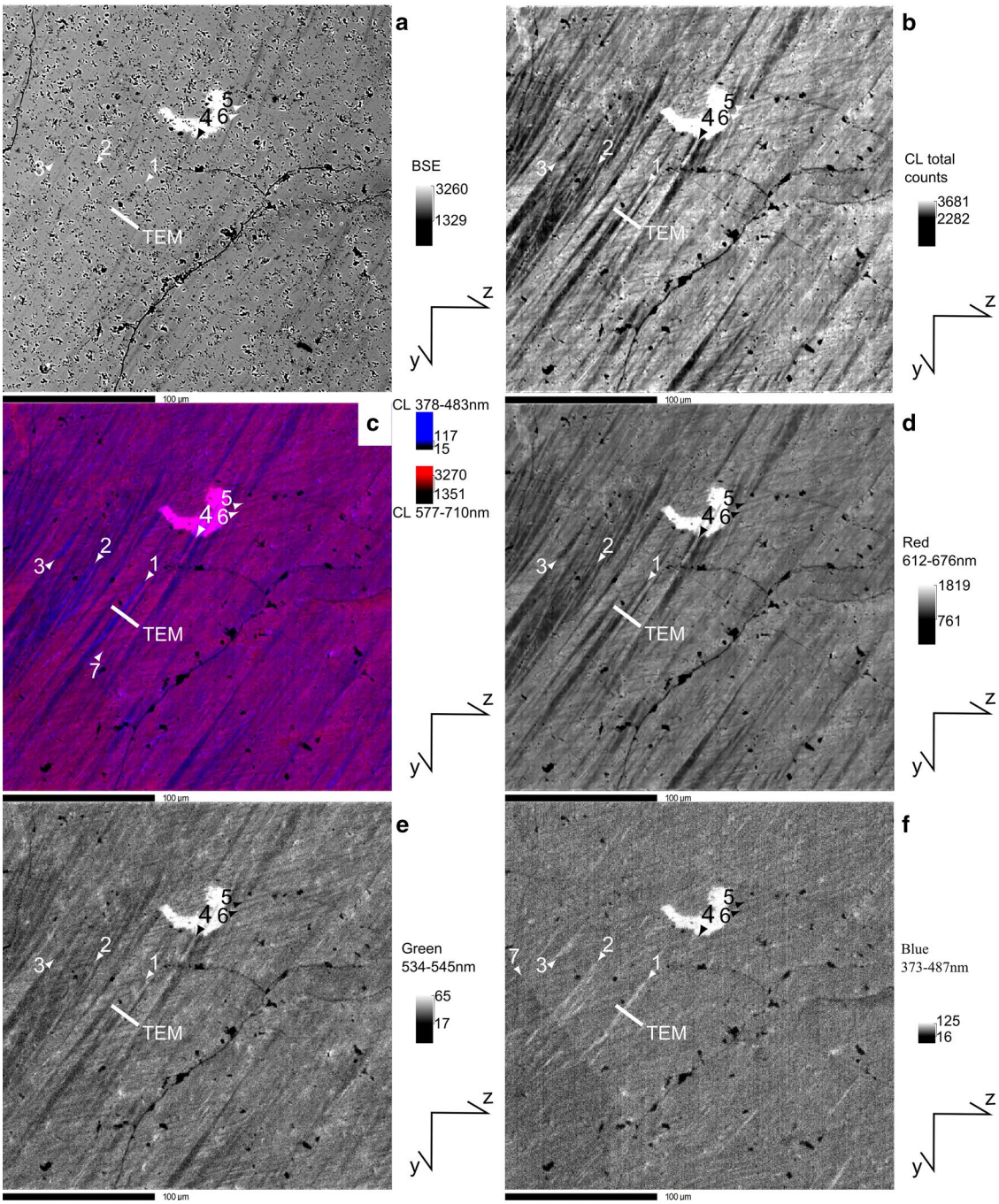

Fig. 10 CL analysis of the sub-rhombohedral FEBs in sample HB08HV13. **a** Forescatter image. **b** Map showing the total CL intensity in a *grayscale*. **c** Map showing a combination of *red* (577–710 nm) and *blue* (378–483 nm) wavelengths. **d–f** Maps displaying the measured intensity of selected wavelength ranges in the spectrogram of the total mapped area. The wavelength ranges in **d–f** are 612–676 nm (*red*), 534–545 nm (*green*) and 373–487 nm (*blue*), respectively. The intensities are displayed in a *grayscale*. The *bright spot* in the *middle* of all maps is caused by a local absence of a C-coating. In the maps (**b–f**), the narrow vertical bands are artefacts resulting from the vertical scanning strategy. The *arrows* serve as reference points for comparison with Fig. 8 and are referred to in the text. The location of the TEM section is indicated with a *thick white solid line, TEM*

in natural quartz, a volume of quartz ranging from about 1.07 to 1.07 $\times$ $10^{-3}\mu m^3$ is needed to provide sufficient water for a round fluid inclusion with a radius of 10 nm (calculation is given in the Online Resource).

Comparing these calculated quartz volumes with the density of fluid inclusions observed in the TEM images (maximum 4 per 1 μm^2, e.g. Fig. 12b–d), we conclude that the nanometre-scale fluid inclusions can be formed

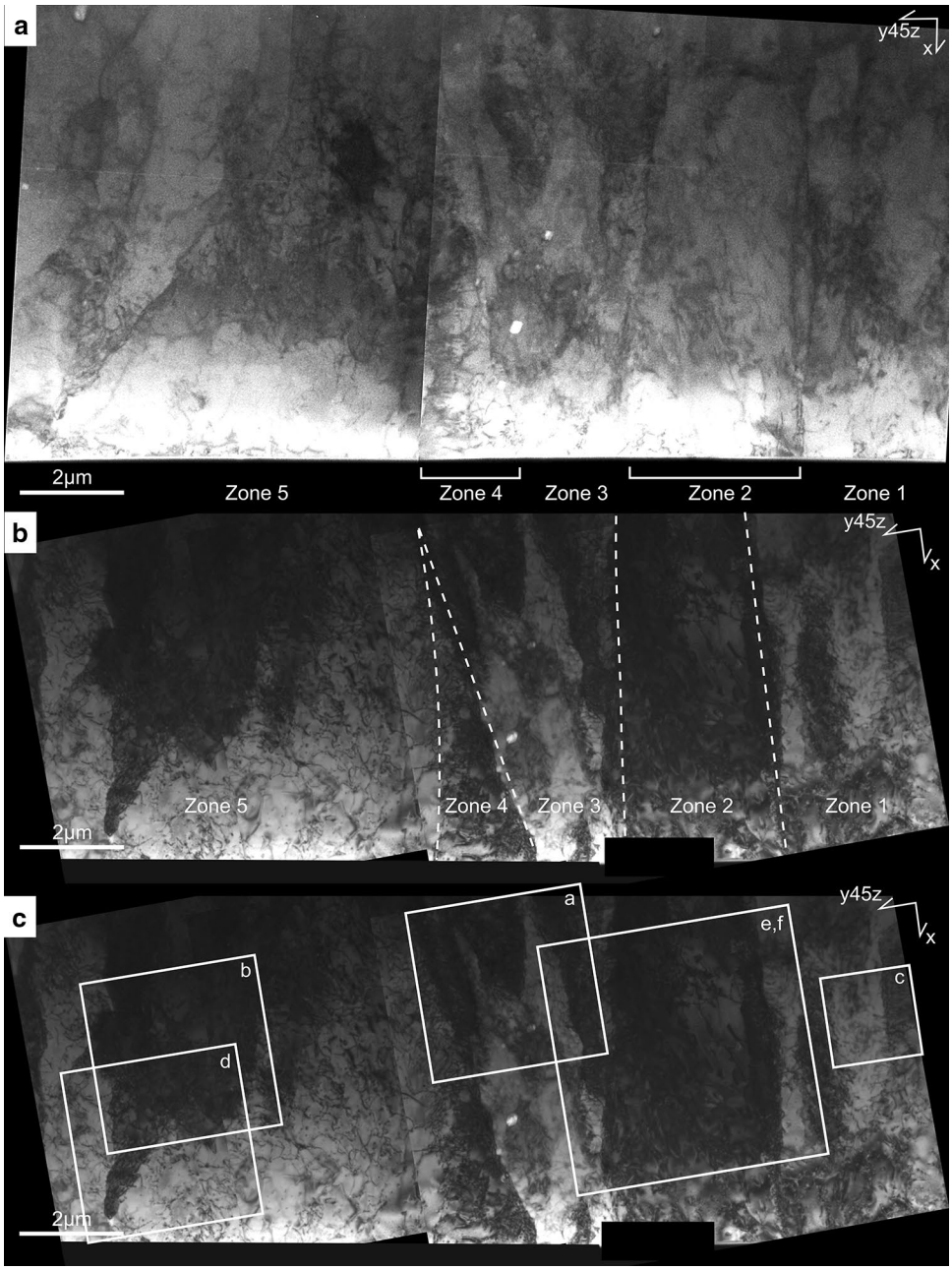

Fig. 11 TEM bright field overview images of the complete TEM foil across the sub-rhombohedral FEBs in sample HB08HV13. **a–c** Overviews with indications of the zones (*dashed lines*) and the locations of the images present in Fig. 12 (*white rectangles*), respectively

from structurally bounded hydroxyl groups, assuming that the quartz contains H/Si concentrations in the ranges used for the calculations in the Online Resource. Fluid inclusions along dislocations can be formed at the same time when quartz with a high water content is deformed by crystal-plastic deformation (McLaren et al. 1983). Alternatively, fluid inclusions can form during static recovery of wet quartz, in which the initial water content concentrates along dislocation cores (Drury 1993). We interpret the larger-scale fluid inclusions (up to 200 nm wide) observed in the TEM foil within the zones as redistributed fluids from nearby fluid inclusions in a FIP.

Correlation between polarized light, EBSD, CL and TEM nanostructures

The combined TEM and EBSD data show the variable extinction observed using polarized light microscopy results from the superimposed effect of the nanostructures present throughout the whole thickness of the thin section. An integrated electron microscopy approach is necessary to

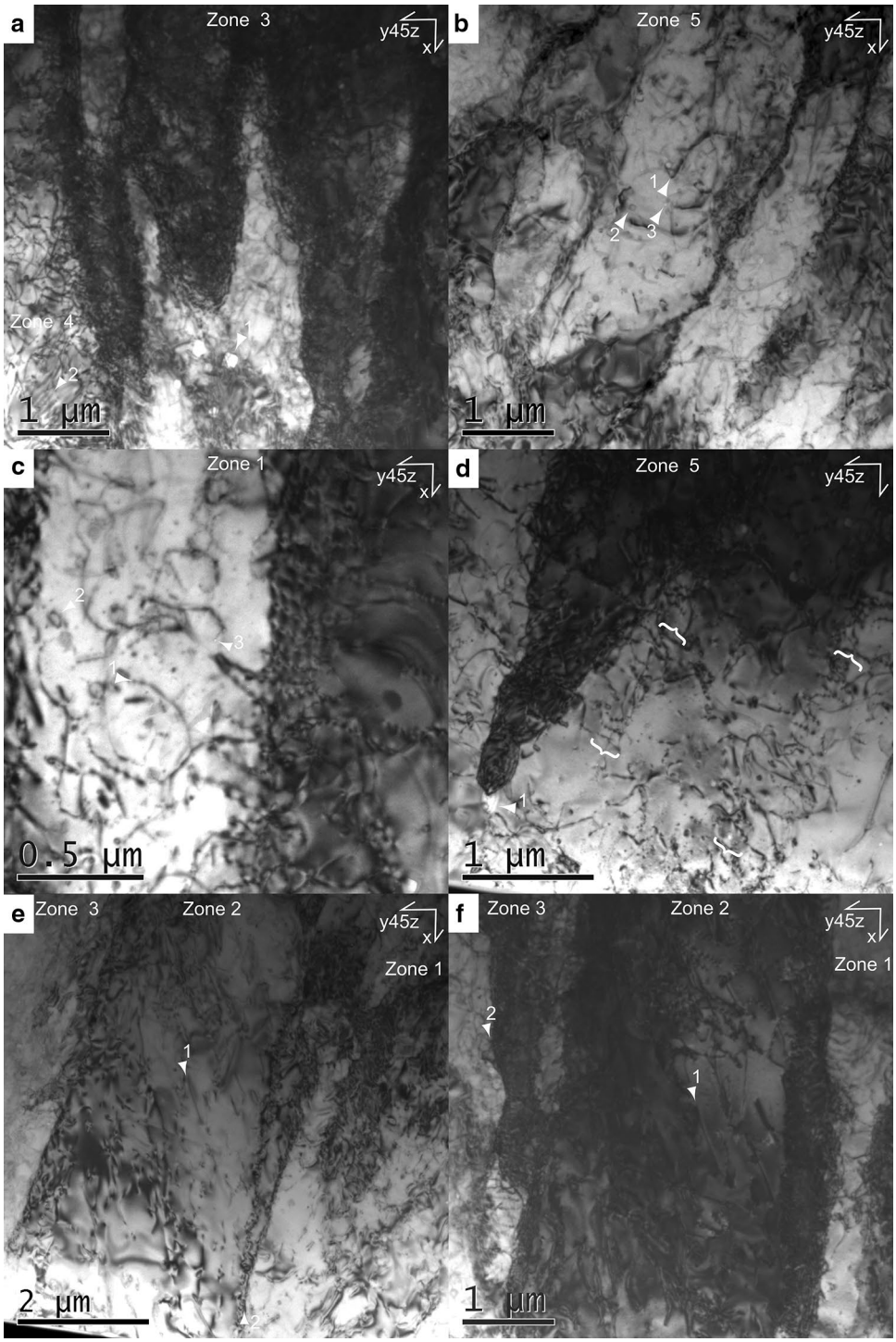

Fig. 12 Bright field images of different zones in the TEM foil across the sub-rhombohedral FEBs in sample HB08HV13. Images were taken with various diffracting conditions, in order to visualize as many dislocations as possible

deduce the deformation mechanisms involved (Twiss 1974; Hamers et al. 2017).

In the literature, CL is generally related to a range of crystal defects in quartz (Götze et al. 2001; Stevens-Kalceff 2009; Götze 2012). For example, CL in the red wavelength range (620–650 nm) has been related to the presence of hydroxyl groups (Si–OH), peroxy linkages (Si–O–O–Si) or strained Si–O bonds that evolve to non-bridging oxygen hole centres ($Si–O^{(0)}$) during electron bombardment (Götze et al. 2001). Non-bridging oxygen centres have also been related to twinning, mechanical deformation, particle bombardment, rapid quartz precipitation (Ramseyer et al. 1988) and the presence of nonbonding alkali ions as Na^+, Li^+ or K^+ (Stevens-Kalceff 2009). Hamers (2013) and Hamers et al. (2016, 2017) have shown that subgrain boundaries and

twin boundaries produce a strong red CL signal, making red-filtered CL imaging a very useful way to image planar defects in quartz, provided the boundaries can be resolved.

Comparing the CL with the TEM analyses of the prismatic FEBs, the association of red CL to the subgrain boundaries and bands of subgrain boundaries is very clear. For the microstructure with two FEB sets, the redder zones 1, 3 and 5 are associated with both a higher dislocation density and a higher fluid-inclusion concentration. Fluids are, however, non-luminescent, so the CL should originate from defects associated with the fluid inclusions. Possibly these fluid inclusions are associated with dislocations as suggested by Viti and Frezzotti (2001) based on TEM analysis. Fluid inclusions can also be associated with a higher concentration of hydroxyl groups (Si–OH).

Blue CL is generally related to the presence of Ti^{4+} and Al^{3+} (and Li^{+}, Na^{+}, K^{+} or H^{+} as charge compensators) (Stevens-Kalceff 2009) and to intrinsic defects (Götze et al. 2001). A concentration gradient in Ti^{4+} across the FEBs in this study is considered unlikely, since Ti^{4+} concentration in quartz is only significant above 500 °C (Müller et al. 2003). A concentration gradient in Al^{3+} cannot, however, be excluded. If so, one possibility is that FEBs are sealed microfractures, with the Al^{3+} originating from the ambient fluid. However, the TEM nanostructures are not consistent with sealed fractures, which usually have very high fluid-inclusion concentrations (Blenkinsop and Drury 1988; Lloyd and Knipe 1992). For the prismatic FEBs, variations in blue CL are interpreted to be related to variations in crystal lattice orientation.

Discussion and conclusion

By using an integrated approach of polarized light microscopy, universal stage microscopy, EBSD, EPMA-CL and TEM, we show that a range of different nanostructures can account for FEB characteristics, such as width and extinction angle, observed using polarized light microscopy. Based on TEM analyses, two new FEB nanostructures are identified in naturally deformed quartz; FEB boundaries consisting of a network of subgrain boundaries, and FEBs as bands with different dislocation density and fluid-inclusion content.

Prismatic FEBs are shown to be bounded by a network of subgrain boundaries. This microstructure is explained by different slip system activity in alternating bands, resulting in bands of tangled dislocations formed during a high-stress deformation stage, that were subsequently recovered during stress relaxation. The prismatic FEB structure is therefore similar to the structure produced by Trepmann and Stöckhert (2013) during "kick and cook" experiments simulating deformation in a seismic–aseismic cycle.

The TEM data of a second example with two FEB sets developed in one grain show that different FEB sets in one grain can be formed by different mechanisms. The finer FEB sets are elongated subgrains, which can be interpreted as recovered slip bands (Drury 1993). The wider FEB set is defined by bands with different dislocation density, fluid-inclusion content and development of elongate subgrains. These wide bands can be interpreted as zones of different plastic strain, associated with the primary growth banding in the quartz grain. We infer that the bands with high dislocation density, water-inclusion content and fine FEBs are high strain bands formed in wet growth bands. In contrast, the bands with lower dislocation density, lower-water-inclusion content and with no fine FEBs are low-strain growth bands with a lower-water concentration. This type of growth controlled deformation microstructure has been recognized in experimentally deformed synthetic quartz (Blacic 1975; Morrison-Smith et al. 1976). This is the first time that this structure has been recognized in naturally deformed quartz.

The occurrence of the different FEB nanostructures, with a range of orientations, including, basal, sub-basal, rhombohedral and prismatic FEBs, suggests that the vein quartz in the HASB has recorded a cyclic deformation, with very high-stress peaks, followed by stress relaxation. This history may be related to seismic–aseismic deformation cycles.

Acknowledgements We would like to thank Prof. Dr. Luiz F.G. Morales and an anonymous reviewer for careful reading of the manuscript and for the useful suggestions that have improved this paper. This research is financially supported by Research Grant OT/11/038 of the Onderzoeksfonds KU Leuven.

References

Bakker R, Jansen JB (1994) A mechanism for preferential H_2O leakage from fluid inclusions in quartz, based on TEM observations. Contrib Miner Petrol 116(1–2):7–20

Becke F (1892) Petrographische Studien am Tonalit der Riesenferner. Tschermak min. u. petr. Mitt

Beugnies A (1986) Le métamorphisme de l'aire anticlinale de l'Ardenne. Hercynica 1:17–33

Blacic JD (1975) Plastic-deformation mechanisms in quartz: the effect of water. Tectonophysics 27(3):271–294

Blenkinsop TG, Drury MR (1988) Stress estimates and fault history from quartz microstructures. J Struct Geol 10(7):673–684

Carter NL, Friedman M (1965) Dynamic analysis of deformed quartz and calcite from the Dry Creek Ridge Anticline, Montana. Am J Sci 263(9):747–785

Christie JM, Ardell AJ (1974) Substructures of deformation lamellae in quartz. Geology 2:405–408

Christie JM, Griggs DT, Carter NT (1964) Experimental evidence of basal slip in quartz. J geol 72(6):734–756

Christie JM, Raleigh CB (1959) The origin of deformation lamellae in quartz. Am J Sci 257:385–407

Den Brok B (1992) An experimental investigation into the effect of water on the flow of quartzite. Geologica Ultraiectina

Depoorter S, Jacques D, Piessens K, Muchez P, Sintubin M (2014) The Mousny massive quartz occurrence – the vestige of a late-orogenic dilational jog in the High-Ardenne slate belt (Belgium). Geol Belg 17(3–4):293–310

Derez T, Pennock G, Drury M, Sintubin M (2015) Low-temperature intracrystalline deformation microstructures in quartz. J Struct Geol 71:3–23

Derez T, Pennock G, Drury M, Sintubin M (2016) Three sets of crystallographic sub-planar structures in quartz formed by tectonic deformation. Earth Planet Sci Lett 442:157–161

Drury MR (1993) Deformation lamellae in metals and minerals. In: Boland JN, Fitzgerald JD (eds) Defects and processes in the solid state: geoscience applications. Elsevier Science Publishers, Amsterdam, pp 195–212

Ferrière L, Morrow JR, Amgaa T, Koeberl C (2009) Systematic study of universal-stage measurements of planar deformation features in shocked quartz: implications for statistical significance and representation of results. Meteor Planet Sci 44(6):925–940

Fielitz W, Mansy JL (1999) Pre- and synorogenic burial metamorphism in the Ardenne and neighbouring areas (Rhenohercynian zone, central European Variscides). Tectonophysics 309:227–256

Götze J (2012) Application of cathodoluminescence microscopy and spectroscopy in geosciences. Microsc Microanal 18:1270–1284

Götze J, Plötze M, Habermann D (2001) Origin, spectral characteristics and practical applications of the cathodoluminescence (CL) of quartz—a review. Mineral Petrol 71(3–4):225–250

Hamers M (2013) Identifying shock microstructures in quartz from terrestrial impacts. New scanning electron microscopy methods, unpublished PhD thesis. University Utrecht

Hamers MF, Pennock GM, Herwegh M, Drury MR (2016) Distinction between amorphous and healed planar deformation features in shocked quartz using composite color scanning electron microscope cathodoluminescence (SEM-CL) imaging. Meteorit Planet Sci 51:1–18

Hamers MF, Pennock GM, Drury MR (2017) Scanning electron microscope cathodoluminescence imaging of subgrain boundaries, twins and planar deformation features in quartz. Phys Chem Miner 44:263–275

Heard HC, Carter NL (1968) Experimentally induced "natural" intragranular flow in quartz and quartzite. Am J Sci 266:1–42

Ingerson E, Tuttle OF (1945) Relations of lamellae and crystallography of quartz and fabric directions in some deformed rocks. Am Geophys Union 26:95–105

Jacques D, Derez T, Muchez P, Sintubin M (2014) Syn- to late-orogenic quartz veins marking a retrograde deformation path in a slate belt: examples from the High-Ardenne slate belt (Belgium). J Struct Geol 58:43–58

Judd JW (1888) The development of a lamellar structure in quartz crystals. Mineral Mag 36:1–8

Kenis I (2004) Brittle–ductile deformation behaviour in the middle crust as exemplified by mullions (former "boudins") in the High-Ardenne slate belt, Belgium. Aardkundige mededelingen, vol 14. Leuven University Press, Leuven

Kenis I, Urai JL, van der Zee W, Hilgers C, Sintubin M (2005) Rheology of fine-grained siliciclastic rocks in the middle crust—evidence from structural and numerical analysis. Earth Planet Sci Lett 233:351–360

Kilian R, Heilbronner R, Holyoke CW, Kronenberg AK, Stünitz H (2016) Dislocation creep of dry quartz. J Geophys Res Solid Earth 121:3278–3299

Lloyd GE (2004) Microstructural evolution in a mylonitic quartz simple shear zone: the significant roles of dauphiné twinning and misorientation. In: Alsop GI, Holdsworth RE, McCaffrey KJW, Hand M (eds) Flow processes in faults and shear zones, vol 224. Geological Society London, London, pp 39–61 **(Special Publications)**

Lloyd GE, Knipe RJ (1992) Deformation mechanisms accommodating faulting of quartzite under upper crustal conditions. J Struct Geol 14:127–143

Lobanov ML, Rusakov GM, Redikultsev AA, Lobanova LV (2013) Formation of special misorientations related to transition bands in structure of deformed and annealed single crystal (110) [001] of Fe-3% Si alloy. Phys Met Metallogr 114(1):27–32

Mainprice D, Jaoul O (2009) A transmission electron microscopy study of experimentally deformed quartzite with different degrees of doping. Phys Earth Planet Inter 172:55–66

McLaren AC, Hobbs BE (1972) Transmission electron microscope investigation of some naturally deformed quartzites. In: Heard HC, Borg IY, Carter NL, Raleigh CB (eds.) Flow and fracture of rocks 16. Geophysical monograph series, American Geophysical Union, Washington DC, pp 55–66

McLaren AC, Phakey PP (1966) Transmission electron microscope study of bubbles and dislocations in amethyst and citrine quartz. Aust J Phys 19:19–24

McLaren AC, Phakey PP (1969) Diffraction contrast from Dauphiné twin boundaries in quartz. Phys Status Solidi 31:723–737

McLaren AC, Retchford JA (1969) Transmission electron microscope study of the dislocations in plastically deformed synthetic quartz. Phys Status Solidi 33(2):657–668

McLaren AC, Retchford JA, Griggs DT, Christie JM (1967) Transmission electron microscope study of Brazil twins and dislocations experimentally produced in natural quartz. Physica Status solidi 19:631–644

McLaren AC, Turner RG, Boland JN (1970) Dislocation structure of the deformation lamellae in synthetic quartz; a study by electron and optical microscopy. Contrib Miner Petrol 29:104–115

McLaren AC, Cook RF, Hyde ST, Tobin RC (1983) The mechanisms of the formation and growth of water bubbles and associated dislocation loops in synthetic quartz. Phys Chem Miner 9(2):79–94

Morrison-Smith DJ, Paterson MS, Hobbs BE (1976) An electron microscope study of plastic deformation in single crystals of synthetic quartz. Tectonophysics 33(1–2):43–79

Müller A, Wiedenbeck M, Kerkhof AMVD, Kronz A, Simon K (2003) Trace elements in quartz—a combined electron microprobe, secondary ion mass spectrometry, laser-ablation ICP-MS, and cathodoluminescence study. Eur J Mineral 15(4):747–763

Neumann B (2000) Texture development of recrystallised quartz polycrystals unravelled by orientation and misorientation characteristics. J Struct Geol 22(11–12):1695–1711

Ord A, Hobbs B (2011) Microfabrics as energy minimisers: rotation recrystallisation as an example. J Struct Geol 33(3):220–243

Oncken O, von Winterfeld C, Dittmar U (1999) Accretion of a rifted passive margin: the Late Paleozoic Rhenohercynian fold and thrust belt (Middle European Variscides). Tectonics 18(1):75–91

Ramseyer K, Baumann J, Matter A, Mullis J (1988) Cathodoluminescence colours in alpha-quartz. Mineral Mag 52:669–677

Savul, Mircea (1948) Les orientations des plans de Böhm dans les cristaux de quartz. Inst Polytech Jassy Bull 3:375–397

Schroyen K, Muchez P (2000) Evolution of metamorphic fluids at the Variscan fold-and-thrust belt in eastern Belgium. Sed Geol 131(3–4):163–180

Stevens-Kalceff MA (2009) Cathodoluminescence microcharacterization of point defects in α-quartz. Mineral Mag 73(4):585–605

Tarantola A, Diamond L, Stünitz H (2010) Modification of fluid inclusions in quartz by deviatoric stress I: experimentally induced changes in inclusion shapes and microstructures. Contrib Miner Petrol 160(6):825–843

Trepmann CA, Stöckhert B (2003) Quartz microstructures developed during non-steady state plastic flow at rapidly decaying stress and strain rate. J Struct Geol 25(12):2035–2051

Trepmann CA, Stöckhert B (2013) Short-wavelength undulatory extinction in quartz recording coseismic deformation in the middle crust—an experimental study. Solid Earth 4(2):263–276

Turner FJ (1948) Note on the tectonic significance of deformation lamellae in quartz and calcite. Eos 29(4):565–569

Twiss RJ (1974) Structure and significance of planar deformation features in synthetic quartz. Geology 2(7):329–332

Van Baelen H (2010) Dynamics of a progressive vein development during the late-orogenic mixed brittle-ductile destabilisation of a slate belt. Examples of the High-Ardenne slate belt (Herbeumont, Belgium). Aardkundige mededelingen, vol 24. Leuven University Press, Leuven

Van Noten K, Van Baelen H, Sintubin M (2012) The complexity of 3D stress-state changes during compressional tectonic inversion at the onset of orogeny. Geol Soc London Spec Publ 367:51–69

Vernooij MGC (2005) Dynamic recrystallisation and microfabric development in single crystals of quartz during experimental deformation. Unpublished PhD Thesis thesis, Eidgenössiche Technische Hochschule Zürich

Vernooij MGC, Langenhorst F (2005) Experimental reproduction of tectonic deformation lamellae in quartz and comparison to shock-induced planar deformation features. Meteorit Planet Sci 40(9/10):1353–1361

Viti C, Frezzotti ML (2001) Transmission electron microscopy applied to fluid inclusion investigations. Lithos 55(1–4):125–138

White S (1973) Deformation lamellae in naturally deformed quartz. Nat Phys Sci 245:26–28